

# Electrocatalytic CO<sub>2</sub> Reduction at Pyridine Functionalized Au Nanoparticles Supported by NanoCOT Electrode

To cite this article: Md Ashaduzzaman et al 2022 J. Electrochem. Soc. 169 116510

View the <u>article online</u> for updates and enhancements.







# Electrocatalytic CO<sub>2</sub> Reduction at Pyridine Functionalized Au Nanoparticles Supported by NanoCOT Electrode

Md Ashaduzzaman, Xin Kang, Lyndi Strange, and Shanlin Pan and

Department of Chemistry and Biochemistry, The University of Alabama, Tuscaloosa, Alabama 35487, United States of America

CO<sub>2</sub> reduction reaction (CO<sub>2</sub>RR) is a promising technique for mitigating global warming and storing renewable energy if it can be obtained with a highly selective, efficient, and durable electrocatalyst. Here, we report CO<sub>2</sub>RR catalyzed by Au nanoparticles (NPs) stabilized by pyridines and pyrimidines (e.g., 2-mercaptopyridine (2Mpy), 4-mercaptopyridine (4Mpy), and 2-mercaptopyrimidine (2Mpym)) on a nanostructured carbon-doped TiO<sub>2</sub> nanowire (NanoCOT) electrode, which has been previously reported by our team for electrocatalytic water oxidation. An online gas chromatography (GC) set-up with improved gaseous product sensitivity with real-time pressure monitoring is used to quantify CO and hydrogen products from the Au NP-modified NanoCOT electrode. High CO selectivity is observed at Au-2Mpy coated NanoCOT electrode. CO<sub>2</sub> reduction products are not observed at bare NanoCOT suggesting CO<sub>2</sub> is reduced at the Au nanoparticle sites of the electrode. Moreover, CH<sub>3</sub>OH is not detected at the Au-Mpy/Mpym NPs during rotating ring disk electrode (RRDE) analysis which implies pyridine attached to the Au NPs has no catalytic effects on CO<sub>2</sub>RR as claimed by others in the literature. A durable complete H-cell using a NanoCOT anode and Au NP-NanoCOT cathode electrodes is assembled for complete water splitting, CO<sub>2</sub>RR, and stability test.

© 2022 The Electrochemical Society ("ECS"). Published on behalf of ECS by IOP Publishing Limited. [DOI: 10.1149/1945-7111/aca17f]

Manuscript submitted September 15, 2022; revised manuscript received October 30, 2022. Published November 18, 2022.

Supplementary material for this article is available online

Global atmospheric CO<sub>2</sub> level has increased 49% in the last two and a half centuries and reached 420.10 ppm at an annual increase of  $\sim$ 2 ppm per year<sup>1</sup> as a result of anthropogenic activities such as industrialization, deforestation, and the combustion of large amounts of fossil fuels to meet the growing energy demand of modern society. CO<sub>2</sub> along with methane, water vapor, nitrous oxide, and ozone are called greenhouse gas that can absorb and emit radiant energy within the infrared range. Greenhouse gases are important for maintaining a livable Earth's surface temperature, however, an uncontrolled increase of these gases in the atmosphere has extreme weather impacts such as heavy precipitation, severe storms, and rising sea level. Thus, there is an urgent need for an efficient and scalable process to capture and store CO2 or transform CO2 into reusable chemical fuels. CO2 can be converted into energy-dense fuel or industrially valuable commodities through diverse routes, such as biochemical,<sup>2</sup> electrochemical,<sup>3</sup> photochemical,<sup>4</sup> thermochemical<sup>5</sup> methods. Electrochemical CO<sub>2</sub>RR into hydrocarbons, oxygenates, or CO is attractive method because of its economic feasibility, engineering control, high current density, and tunable specificity of reduction products. Additionally, electrochemical CO<sub>2</sub>RR coupled with renewable energy sources such as solar, tidal, or wind energy can serve as a scalable energy storage system.<sup>6</sup> Electrochemical CO<sub>2</sub>RR is challenging because of the high energy required to break the strong C=O bond and slow reaction kinetics. Although CO<sub>2</sub>RR steps are thermodynamically more favorable than hydrogen evolution reactions (see Table I), selectivity and reaction rates of these CO<sub>2</sub>RR reactions are highly sensitive to electrode materials. For example, CO<sub>2</sub> molecule needs to coordinate with the solid electrode surface to receive electrons to form a bent anion radical, which is necessary for the process of transferring the first electron and forming CO<sub>2</sub>• radical anion. Furthermore, an overpotential of a couple hundred millivolts in addition to the thermodynamic potential is required to initiate the reduction reaction at a considerable rate. Some CO<sub>2</sub>RR steps need proton-assisted electron transfer mechanism to bypass high activation energy. However, proton reduction reaction can compete with CO<sub>2</sub>RR, thus a catalyst with proton suppression capability is essential for CO<sub>2</sub> reduction in an aqueous solution. Finally, CO<sub>2</sub> can be transformed into a mixture

<sup>z</sup>E-mail: span1@ua.edu

of products depending on the number of proton-electron transfer during electrocatalysis. Thus, catalytic engineering and design have been essential for catalysts development that can effectively reduce  $CO_2$  at low overpotential (cell voltage  $\leq 1.8 \text{ V}$ ) with high current density ( $\geq 350 \text{ mA cm}^{-2}$ ), product selectivity ( $\geq 80\%$  for a specific product) and long-term stability ( $\geq 80000 \text{ H}$ ) in various chemical environments and can achieve industrial requirements.  $^{6,8}$ 

Remarkable efforts have been made to search CO2RR electrocatalysts. Transition metals (e.g., Au, Ag, 10 Cu11), metal oxides (e.g. CuO12 and ZnO13), bimetallic oxides, and semiconducting materials<sup>14</sup> have been thoroughly investigated. The presence of vacant orbitals and active d-electrons in transition metals and metal oxides energetically facilitates metal-CO<sub>2</sub> bond formation, stabilizes intermediates, and assists the desorption of the reduced species. However, metals are scarce and expensive which limits their use in cost-effective catalyst synthesis for the scalable CO2 reduction process. Thus, metal NPs are utilized to modify a conductive surface to obtain a catalyst for CO<sub>2</sub>RR. <sup>16</sup> Various metals have been used for surface modification to improve  $CO_2$  reactivity and selectivity including  $Cu, ^{17}$   $Au^{18}$  and  $Ag.^{19}$  Among these, Au NPs can selectivity reduce CO<sub>2</sub> to CO because of the relatively weak binding towards the \*CO intermediates which limits its transformation to \*CHO.<sup>20</sup> Titanium dioxide (TiO<sub>2</sub>) is an attractive choice as a catalyst due to its high chemical stability, low-cost, facile fabrication, nontoxicity, photoelectrochemical activity, and photocorrosion resistivity. However, the application of TiO<sub>2</sub> as a catalyst for CO<sub>2</sub>RR is largely limited by its poor electrical conductivity, low specific surface area, and large band gap (3.0 eV for Rutile and 3.2 eV for anatase).<sup>21</sup> The electrical conductivity of TiO<sub>2</sub> can be improved by doping with metal and nonmetal heteroatoms. Metal doping introduces empty orbitals by replacing titanium atoms in the lattice, which produces an n-type semiconductor and lowers the band gap.<sup>2</sup> However, metal-doped TiO<sub>2</sub> frequently suffers from photocorrosion and chemical instability due to the leaching of doped metals.<sup>2</sup> Alternatively, non-metal doping is believed to be less expensive, more durable, and more stable. Non-metal doping introduces occupied orbitals above the valance band (VB) by replacing oxygen atoms of the crystal, resulting narrow band gap with the formation of p-type semiconductor.<sup>24</sup> Carbon and carbon based materials (e.g., graphene, carbon nanotubes, etc.) are widely used as doping agents due to their large electron storage capacity, charge carrier separating efficiency, and improved conductivity.<sup>25</sup> Our team previously reported carbon-doped TiO2 nanowire (NanoCOT) electrode formed

<sup>&</sup>lt;sup>a</sup>Present address: Energy and Environment Directorate, Pacific Northwest National Laboratory, Richland, Washington 99354, USA.

Table I. Products of CO <sub>2</sub> reduction with their correspon	nding equation, transferred el	lectron numbers, and standard potential.
---	--------------------------------	--

Product	Reaction	n	E <sup>0</sup> (V vs NHE)
Carboxylate anion	$\mathrm{CO_2} + \mathrm{e^-}  ightarrow \mathrm{CO_2}$ .	1	-1.97
Carbon monoxide	$\mathrm{CO_2} + 2\mathrm{H^+} + 2\mathrm{e^-} \rightarrow \mathrm{CO} + \mathrm{H_2O}$	2	-0.51
Formic acid	$CO_2 + 2H^+ + 2e^- \rightarrow HCOOH$	2	-0.58
Oxalate	$2\text{CO}_2 + 2\text{H}^+ + 2\text{e}^- \rightarrow \text{H}_2\text{C}_2\text{O}_4$	2	-0.87
Methanol	$\mathrm{CO_2} + 6\mathrm{H^+} + 6\mathrm{e^-} \rightarrow \mathrm{CH_3OH} + \mathrm{H_2O}$	6	-0.39
Methane	$CO_2 + 8H^+ + 8e^- \rightarrow CH_4 + 2H_2O$	8	-0.24
Ethanol	$2\text{CO}_2 + 12\text{H}^+ + 12\text{e}^- \rightarrow \text{C}_2\text{H}_5\text{OH} + 3\text{H}_2\text{O}$	12	-0.33
Ethane	$2\text{CO}_2 + 14\text{H}^+ + 14\text{e}^- \rightarrow \text{C}_2\text{H}_6 + 4\text{H}_2\text{O}$	14	-0.27
Hydrogen	$\rm H_2O + 2e- \rightarrow 2OH^- + H_2$	2	-0.41

by a high-temperature carbon transformation of  $TiO_2$  nanowire in a mixed  $CH_4/H_2/N_2$  atmosphere to obtain reduced Ti ( $Ti^{1+}$ ,  $Ti^{2+}$ ,  $Ti^{3+}$ ) defect states for electrocatalytic water splitting. There is no report on how such doping would improve selectivity and efficiency of  $CO_2RR$ . Additionally, there are several reports of  $CO_2$  conversion into  $CH_3OH$  assisted by pyridine molecules at metal catalysts such as on Pt, p-GaP, p-CuInS $_2$  and Pt/Au. However,  $CH_3OH$  production was not observed in numerous studies in the presence of pyridine at Pt, Au, Ag electrode as summarized in Table II. Additionally, Fang et al. demonstrated electrochemical  $CO_2$  reduction at the Au surface functionalized with three thiol-tethered ligands: 2-mercaptopropanoic acid, 4-pyridinylethanemarcaptan, and cysteamine, of various pKa values.

Here, we report CO<sub>2</sub>RR activities of Au NPs stabilized by pyridines and pyrimidines (e.g., 2-mercaptopyridine (2Mpy), 4-mercaptopyridine (4Mpy), and 2-mercaptopyrimidine (2Mpym)) on a NanoCOT electrode. CO2RR at Au-2Mpy/NanoCOT catalyst with 51.16% faradaic efficiency for CO production at −1.38 V vs RHE is obtained. Au-2Mpym/NanoCOT exhibits the least CO<sub>2</sub>RR at all applied potentials with CO faradaic efficiency of 19.28% at -0.88 V vs RHE. Furthermore, competition between H₂ and CO production at each catalyst was observed at all electrodes. No detectable CH<sub>3</sub>OH was obtained with Au-Mpy/Mpym NPs in contrast to the reported results with pyridine-catalyzed CO<sub>2</sub>RR. 40 Additionally, an electrochemical CO<sub>2</sub>RR system with Au-2Mpy/ NanoCOT cathode and bare NanoCOT anode showed improved catalytic performance with a current density of  $\sim$ 15 mA cm<sup>-2</sup> up to 108 C charge collection. An improved and sensitive online GC system for gaseous product analysis directly from the air-sealed Hcell with a real-time pressure monitoring system for leakage investigation is also reported for systematic product identification and quantification.

#### **Experimental**

Chemicals.—The following chemicals were used as received without further purifications: Gold Chloride (HAuCl<sub>4</sub>.3H<sub>2</sub>O, BWR), 4Mpy (C<sub>5</sub>H<sub>5</sub>NS, Sigma-Aldrich), 2Mpy (C<sub>5</sub>H<sub>5</sub>NS, Beantown Chemical), 2Mpym (C<sub>4</sub>H<sub>4</sub>N<sub>2</sub>S, Acros organics), Potassium bicarbonate (KHCO<sub>3</sub>, Fisher Scientific), Sodium borohydride (NaBH<sub>4</sub>, Fisher Scientific), Hydrochloric Acid (HCl,36.5%–38%, BWR), Nafion solution (5% in ethanol, Clean Fuel Cell Energy, LLC), Iron (III) nitrate nonahydrate (Fe(NO<sub>3</sub>)<sub>3</sub>.9H<sub>2</sub>O, ACROS), methanol (CH<sub>3</sub>OH, VWR) and Titanium plate (Ti, 99%, 0.5 mm in thickness). Gas mixture of 16% CH<sub>4</sub> and 20.51% H<sub>2</sub> balanced with N<sub>2</sub>, and 99.999% CO<sub>2</sub> was purchased from Airgas.

Au-Mpy/Mpym NPs synthesis.—Au- Mpy/MPym NPs were synthesized by following a similar procedure reported previously. 41 0.067 g of 2-Mpy was dissolved in 10 ml methanol (0.6 mmol) in a 20 ml capped glass bottle (Fig. 1). Then, 6 ml of 50 mM HAuCl<sub>4</sub>· 3H<sub>2</sub>O in methanol (0.3 mmol) was added to the solution under vigorous stirring at room temperature. Freshly prepared 3 ml of aqueous NaBH<sub>4</sub> solution (3 mmol) was added to the solution dropwise

under vigorous stirring. An immediate color change of the solution from yellow to black was observed. The solution was kept for 3 h with continuous stirring at 1200 RPM to achieve thermodynamic equilibrium. Solvents were then evaporated off under steady  $N_2$  gas flow, and products were washed three times with diethyl ether and deionized (DI) water to remove residue Mpy/MPym. The cleaned products were vacuum-dried for 24 h at room temperature. Au-2MPym and Au-4Mpy NPs were prepared following the same procedure.

NanoCOT fabrication.—The fabrication process of NanoCOT nanowires was reported in our previous work.  $^{26}$  Briefly, 1.5 cm imes1.0 cm Ti plates were successively cleaned with ethanol, acetone, and DI water by sonicating for 10 min in each reagent. The air-dried Ti plates were loaded into a 45 ml Teflon-lined stainless-steel autoclave containing 20 ml of 0.6 M HCl solution. The autoclave was then heated at 190 °C for 12 h. After cooling to room temperature, the as-prepared Ti NW samples were cleaned with DI water and annealed in air at 450 °C for 10 h to form the surface oxidized TiO2 NW substrate. The thermally annealed TiO2 NW substrates were treated with 0.5 M Fe(NO<sub>3</sub>)<sub>3</sub> solution for 30 min, washed with acetone, and dried in air to enhance carbon doping. The Fe catalyst-coated substrates were horizontally placed into a quartz boat with a quartz plate cover on top to allow sufficient mixture gas retention time for the carbon transformation reaction. The boat was loaded in a tube furnace (1100, MTI Corporation, Richmond, CA). The chamber was purged by three vacuum/N2 purge cycles to discard oxygen from the furnace, followed by a constant N2 gas flow up to 700 °C. The furnace temperature was set to 900 °C with a ramp rate of 50 °C min<sup>-1</sup> and a dwell time of 1 h. At  $\sim$ 700°, the N<sub>2</sub> gas was turned off and the CH<sub>4</sub>/H<sub>2</sub>/N<sub>2</sub> gas mixture (16% CH<sub>4</sub> and 20.51% H<sub>2</sub> balanced with N<sub>2</sub>) was turned on at a flow rate of  $\sim$ 200 sccm. After the carbon transformation reaction, the furnace was allowed to cool under CH<sub>4</sub>/H<sub>2</sub>/N<sub>2</sub> flow until the temperature of the furnace reached  $\sim 700$  °C. At this temperature, the mixed gas flow was turned off and N2 flow was turned back on. The samples were allowed to cool to room temperature in a N<sub>2</sub> steam before being removed from the furnace.

Au-Mpy/MPym NP coated NanoCOT.—1.2 mg of powdered Au-2Mpy NPs were dissolved in 1 ml DI water and sonicated for  $\sim\!1\,h$  to get a well-dispersed NPs solution. Then, Au-2Mpy/NanoCOT electrodes were fabricated by drop coating 200  $\mu$ l Au-2Mpy NPs on a bare NanoCOT substrate. The drop-coated electrode was dried in an ambient atmosphere with slow solvent evaporation by keeping it in the air for 6–8 hours. Au-2Mpym/NanoCOT and Au-4Mpy/NanoCOT electrodes were prepared using the same procedure.

*Electrochemical characterizations.*—Rotating ring-disk electrode (RRDE), and cyclic voltammetry (CV) measurements were carried out using an electrochemical workstation (CHI 760C, CH Instruments). The RRDE voltammograms were recorded on a RRDE configuration (ALS Co. Ltd., Japan) with a glassy carbon (GC) disk electrode surrounded by a Pt ring electrode with a Polytetrafluoroethylene

Journal of The Electrochemical Society, 2022 169 116510

27

35

36

37

38

39

	Pyridine			D 1	Faradaic Efficiency/	ъ. с
Catalyst	Surface adsorbed	Solution	Applied potential	Products	Concentration	References
Pt		pyridine	-0.5 to $-0.8$ V vs Ag/AgCl	CH <sub>3</sub> OH	10%	28
p-GaP		10 mM pyridine	-0.52  V	CH₃OH	100%	29
Polycrystalline Pt		4-10  mM pyridine	-0.55 V to $-0.96$ V vs NHE	No CH <sub>3</sub> OH/HCOOH	_	30
p-CuInS <sub>2</sub>	Pyridine layer	_	-0.59  V	CH₃OH	1.6 mM	31
$FeS_2$	_	10 mM pyridine	−1.1 V SCE	НСООН	2.7%	32
CdTe	_	5-30 mM pyridine	-0.6  V	НСООН	43.6%-60.7%	33
Au/py/CNT	4-amino pyridine	_	-0.58~V to $-0.98~V$ vs RHE	CO	93%	34

-0.6 V to -1.1 V vs RHE

-0.67 vs RHE

-0.8 V vs RHE

-1.1 vs Ag/AgCl

 $-0.75 \text{ V to } -1.2 \text{ V vs Fc}^{0/+}$ 

-0.20 vs Ag/AgCl

HCOO-/CO

Dihydrogen

CH<sub>3</sub>OH/HCOOH

CO/H<sub>2</sub>

CO/H<sub>2</sub>

CH<sub>3</sub>OH

22%/35%

36%/8%

5 ppm

Table II. Pyridine catalyzed CO2 reduction products and faradaic efficiency at various metals and semiconductor electrodes.

10 mM pyridine

2mercaptopropanoic acid/4 pyridylethyl-

mercan/Cystine

Poly(4vinylpyridine

Amino pyridine

Dihydropyridine

2 pyridine thiols

Au

Au

Ag

Au

Pt

Pt/Au nanoparticle



Figure 1. Schematic diagram of Au-Mpy/Mpym nanoparticle synthesis.

(PTFE) insulation layer in between two electrodes. The geometric area of the Pt ring electrode was  $0.75 \text{ cm}^2$  (ID = 0.5 cm and OD = 0.7 cm). A central GC disk electrode having a geometric area of 0.5 cm<sup>2</sup> was used as a substrate to deposit Au Mpy/Mpym NPs. Before catalyst deposition, the RRDE was initially polished with a 0.3  $\mu$ m alumina (Buehler) slurry on a nylon pad and subsequently with 0.05  $\mu$ m slurry on a micro-cloth (CHI Instruments) and cleaned with acetone and DI water respectively by ultrasonication for 2 min. Additionally, the Pt ring electrode was electropolished using 0.1 M HClO<sub>4</sub> acid solution by running ~100 cycles of CVs until stable hydrogen adsorption and desorption peak on Pt was observed. 1.2 mg of the as-prepared Aupyridine/pyrimidine NPs were taken in 1 mL DI water and 50  $\mu$ l Nafion solution was added. Then the solution was sonicated for  $\sim$ 1 h to achieve a well-dispersed NP solution. After that,  $6 \mu l$  of welldispersed Au-Mpy/Mpym NPs were drop coated on the GC disk electrode (GCE) and dried with a rotation of 300 RPM to get a nice circular shape and maximum surface coverage. For testing CO<sub>2</sub>RR activities, 0.1 M KHCO<sub>3</sub> electrolyte solution was pressure saturated with CO<sub>2</sub> gas using 35 psi pressure in a closed container before the test. All the RRDE CVs were recorded at room temperature with a rotation frequency of 3000 RPM in a four-electrode system: Au-Mpy/ Mpym NPs deposited GCE was 1st working electrode, Pt ring electrode was the 2nd working electrode, Ag/AgCl as the reference electrode, and a spiral Pt wire as the counter electrode. In each case, multiple cycle CVs were performed at the ring electrode starting from the open circuit potential ~0.85 V vs RHE in a range of 0.01 V to 1.51 V vs RHE while a constant potential was applied to GCE. During the experiment, CO2 was reduced continuously at the disk electrode depending on the applied potential and the ring electrode detected the CO<sub>2</sub> reduction products from its oxidation potential and corresponding current response. CVs of the bare NanoCOT and Au-Mpy/Mpym coated NanoCOT were carried out in the same procedure stated above using pressurized CO<sub>2</sub> saturated 0.1 M KHCO<sub>3</sub> solution in a threeelectrode system, where Au-Mpy/Mpym NPs-modified NanoCOT was the working electrode, Ag/AgCl as the reference electrode and spiral Pt wire was the reference electrode. All the potentials in this work were measured against Ag/AgCl (sat'd KCl) reference electrode and are reported vs reversible hydrogen electrode (RHE) using the following equation:

$$E_{RHE} = E_{Ag/AgCl} + 0.059pH + E_{Ag/AgCl}^{0}$$
 [1]

Where,  $E_{RHE}$  is the converted potential vs Ag/AgCl,  $E_{Ag/AgCl}$  is the experimental potential measured and  $E^{0}_{Ag/AgCl}$  is the standard potential of Ag/AgCl which is 0.1976 V at 25 °C.

Gas product analysis with GC.—Gaseous products were investigated using a gas chromatography (GC) system with a Thermal Conductivity Detector (8610C, SRI Instruments, INC) connected to an air-sealed two-compartment electrochemical cell. A proton exchange membrane (Nafion 117 membrane) was used to separate anode and cathode compartments to avoid electrolyte and chemical crossing. The H-shape electrochemical cell (H-cell) consisted of a three-electrode system in which the working electrode was prepared by drop coating and air drying of 200  $\mu$ l of Au-Mpy/Mpym NPs on a 1.5 cm × 1 cm NanoCOT substrate. A graphite rod and an Ag/AgCl (sat'd KCl) were used as the counter and reference electrodes, respectively. For electrolyte preparation, 250 ml 0.1 M KHCO<sub>3</sub> solution was initially saturated with CO2 using 35 psi in an airsealed Teflon container. Before the electrolysis, the CO<sub>2</sub>-saturated 0.1 M KHCO<sub>3</sub> solution in the air sealed-cell was purged with CO<sub>2</sub> for another 30 min at a flow of 15 ml min<sup>-1</sup> to flush out air from the headspace volume of the H-cell. Then, the CO2 flow was stopped and an aliquot of gas from the headspace volume was directly passed through the GC sample holder using a peristaltic pump to check for the presence of H<sub>2</sub> before CO<sub>2</sub>RR. During electrolysis, a constant potential was applied by using a potentiostat (PWR-3, BAS power module) while the current and integrated electrolysis charge were recorded with a LabVIEW program through a NI digital multimeter device USB-4065. A 100 psi pressure transducer sender sensor connected to the gas outlet of the air-sealed electrochemical cell was used to monitor pressure change via a Keithley 2400 multimeter before and during the experiment. Figure 2 shows the real-time pressure change during electrolysis of CO<sub>2</sub> monitored with a LabVIEW program. Pressure in the electrochemical cell was intentionally kept slightly higher than the atmospheric pressure to monitor system leakage before catalysis. The setup was left for 10-15 min to achieve a stable pressure inside the cell which

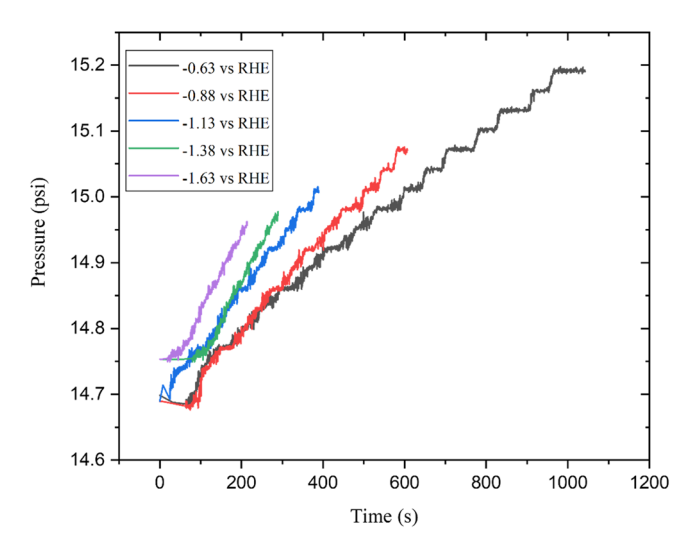


**Figure 2.** Real-time steady pressure increase monitoring with LabVIEW program inside the electrochemical cell during CO<sub>2</sub> electrolysis at different potentials.

indicates the seal was adequate before applying reduction potential. After that, a constant negative potential was applied at the working electrode until a total 2C charge has been collected. No stirring was applied during the electrolysis to avoid pressure fluctuation resulting from  $CO_2$  gas desorption from electrolytes. The steady increase of pressure in the electrochemical cell was observed during the electrolysis because of gaseous product ( $H_2$  and CO) formation. The potential was stopped after 2C of charge accumulation and the gaseous products were passed through the GC system by using a peristaltic pump to obtain a GC chromatogram. Figure 3 represents the schematic diagram of the online GC set-up connected to a two-compartment electrochemical cell. A real image of the laboratory setup is attached in the supplementary section (Fig. S9). A standard gas containing 1%  $H_2$ , 1%  $CH_4$ , 1% CO, and 1%  $CO_2$  balanced by  $N_2$  was purchased from Airgas and used for GC calibration. The

faradaic efficiency of the gaseous products was calculated by using the following equation:

Faradaic Efficiency, FE% 
$$= \frac{1000 \frac{mL}{L} \times \frac{22.4L}{mol} \times n \times 96485C/mol}{v\% \times V_{headspace} \times Q_{charge\ of\ electrolysis\ (C)}} \times 100\% \quad [1a]$$

Electrode characterization.—Electrodes of Au-Mpy/Mpvm NPs coated NanoCOT catalysts were fully characterized using Apreo Scanning Electron Microscopy (SEM). The sample for SEM imaging was prepared by drop coating 200  $\mu$ l of a solution containing NPs on NanoCOT substrate and allowing the solvent to evaporate at ambient temperature and pressure. Transmission Electron Microscopy (TEM) images were recorded using FEI Tecnai F-20 TEM. The sample was prepared by drop coating a diluted solution containing NPs on a carbon-coated copper grid (300 mash) and keeping the sample for 24 h to evaporate the solvent. Matrix-assisted laser desorption ionization time of flight (MALDI-TOF) mass spectrometry experiments were conducted on a Bruker Daltonics rapifleX mass spectrometer equipped with a smartbeamTM 3D laser in negative and positive mode. FlexControl 4.0 software was used to examine individual data point mass spectra. Samples for the MALDI-TOF experiment were prepared by drop coating  $10 \,\mu l$  of AuNP solution on a stainless steel target. CHCA and Phosphorous red mixture was used for MS system calibration.

#### **Results and Discussion**

NPs solubility, stability and electrode morphology.—All onephase freshly synthesized NPs were dark black in color. NPs were soluble in polar solvents such as DI water and methanol but insoluble in nonpolar organic solvents such as diethyl ether and toluene. Depending on modifying Mpy/Mpym molecules, NPs showed different stability in the solution. 2Mpy modified Au NPs showed the highest stability with a black color solution even after months. However, 2Mpym modified Au NPs solution turns dark brown or blue after keeping it for several days indicating

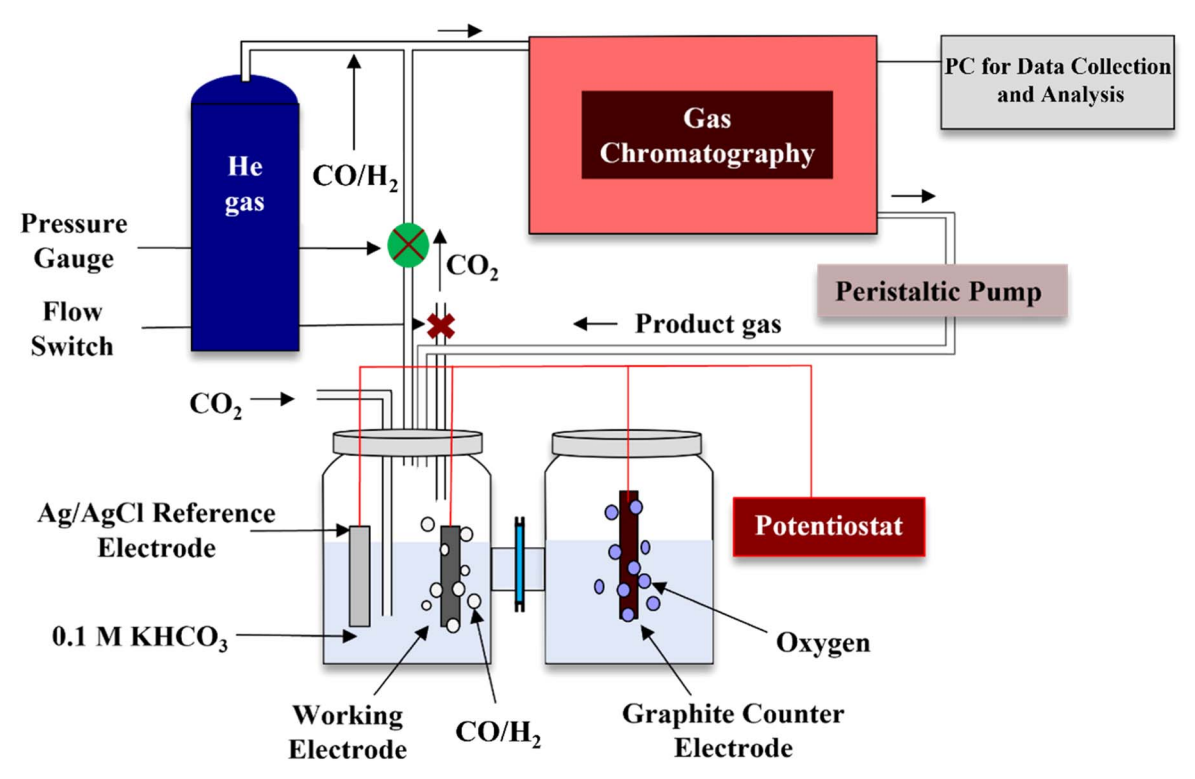


Figure 3. Schematic diagram of online GC setup connected with air-sealed electrochemical cell for gaseous product analysis.

agglomeration of the NPs.<sup>42</sup> The lowest stability was observed for 4Mpy modified Au NPs which precipitate from the solution after 1–3 h and form black flocculate due to large 3D aggregation.

SEM images of the Au-2Mpy coated NanoCOT shows welldispersed NPs on nanoCOT substrate (Fig. 4a) compared to Au-2Mpym (Fig. 4b) and Au-4Mrpy (Fig. 4c) coated NanoCOT substrate. However, NPs are not equally distributed at the NanoCOT surface, which might be due to the rough NanoCOT surface and strong surface tension of water solvents forcing the NP's diffusion and aggregation during solvent evaporation of the drop coating process. Au-4Mpy coated NanoCOT forms large 3D aggregates after solvent evaporation, consistent with our previous observation of precipitate from solvent. TEM images show approximately circular-shaped Au-2Mpy NPs (Fig. 4d) with an average particle diameter of 4.54 nm (Fig. 4g) and is the smallest among all three samples. The 2Mpym modified NPs (Fig. 4e) have a diameter of 4.94 nm (Fig. 4h). Au-2Mpym NPs displayed a strong inclination to form 2D aggregates on TEM grid and NanoCOT substrate (Fig. 4b). The formation of 2-Mpym 2D aggregates was attributed to hydrogen bond formation between neighboring molecules at Au surface. Finally, Au-4Mpy formed the largest NPs (Fig. 4f) with an average diameter of 10.66 nm (Fig. 4i). Au-4Mpy NPs are unstable and form large 3D microstructures. The 3D agglomeration of

Au-4Mpy is attributed to the formation of disulfide dimers among neighboring NPs with free sulfur groups.<sup>41</sup>

UV-vis spectroscopy and mass-spectrometry.—UV-visible (UV-vis) spectroscopy of the as-prepared Au NPs showed a broad surface plasmon absorption peak as shown in Fig. 5. The broad absorption spectrum indicates the formation of NPs agglomeration as shown by TEM images of the aggregated NPs. In the MALDI-TOF mass spectra of 2-Mpy modified Au nanoparticles, the expected,  $[M-H]^-$  109.9 and  $[M + H]^+$  111.9 ions were observed in negative and positive ion spectra, respectively, which are derived from 2-Mpy (Figs. 6a and 6b). Au, Au<sub>2</sub>, Au<sub>3</sub> cluster ions (m/z 197.0, 394.0, 591.0) were observed in the negative ion spectrums. [M-H] and  $[M + H]^+$  ions for 2-Mpym modified Au nanoparticles was observed at m/z 110.9 and 112.9 respectively in negative and positive ion mode as shown in Fig. S6a. Additionally, 4-Mpy modified Au nanoparticles showed strong peaks at m/z 417.0 and 724.0 which are assigned to  $[Au(C_5H_3NS)_2]^-$  and  $[Au_2(C_5H_4NS)_3]^-$  ions respectively, along with characteristic  $[M-H]^-$  and  $[M+H]^+$ ion peak at m/z 109.9 and 111.9 (Fig. S6b). Thus, mass spectrometry confirms the presence of small Mpy/Mpym molecules and fragmented molecules attached Au cluster in the synthesized AuNPs sample as summarized in Table III.

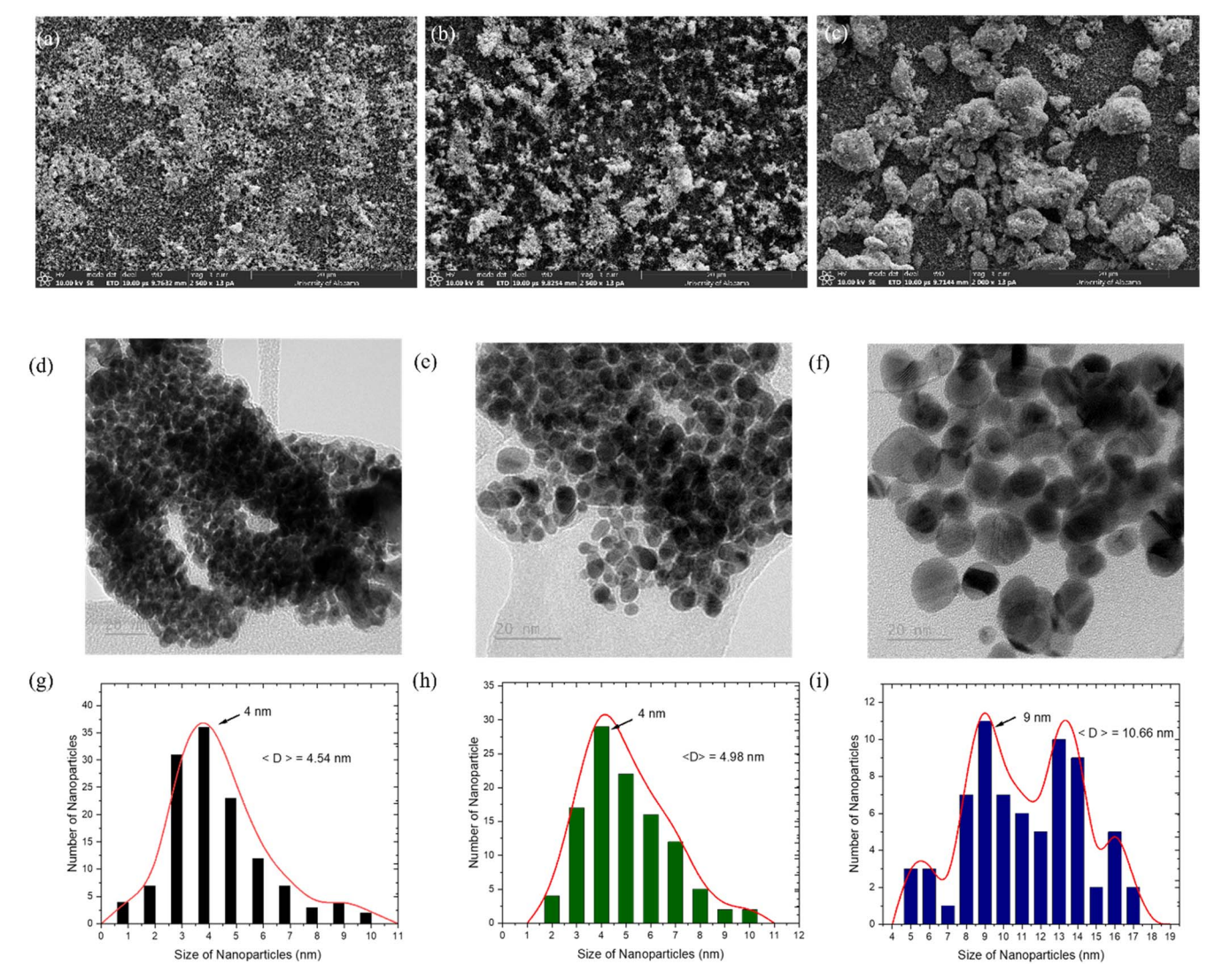
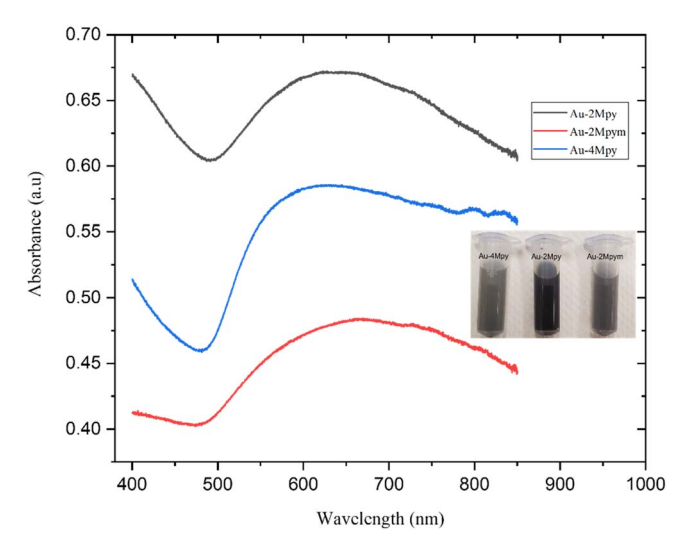


Figure 4. SEM images of Au-2Mpy (4.a), Au-2Mpym (4.b) and Au-4Mpy (4.c) drop coated NanoCOT substrate. TEM images of Au-2Mpy (4.d), Au-2Mpym (4.e) and Au-4Mpy (4.f) NPs. Particle size distribution of Au-2Mpy (4.g), Au-2Mpym (4.h) and Au-4Mpy (4.i) NPs measured from TEM micrograph using Image J software.



**Figure 5.** UV–vis absorption spectrum for Au-2Mpy (black line), Au-4Mpy (blue line) and Au-2Mpym (red line). Inset image is the picture of assynthesized Au-4Mpy, Au-2Mpy, and Au-2Mpym NPs.

Electrochemistry characterizations.—CVs of bare NanoCOT and Au-Mpy/Mpym NPs coated NanoCOT electrodes were collected in 0.1 KHCO<sub>3</sub> solutions purged with CO<sub>2</sub> and N<sub>2</sub> gas respectively for 20-30 min. The oxygen levels in the solutions were expected to be low although not similar. CVs indicate increased catalytic activity in CO<sub>2</sub> purged solution compared to the N<sub>2</sub>-purged solution with an enhanced current density (Fig. S1). Figure 7 shows that the onset potential for bare NanoCOT electrode in CO2 purged solution is around  $-0.6 \,\mathrm{V}$  vs RHE. However, the onset potential shifted anodically at about 200 mV after Au NPs coating. The shifting of the onset potential is barely a result of increased catalyst's surface area after Au-NPs coating at the substrate because our previous reports confirmed the high surface area of NanoCOT substrate due to the presence of carbon doped TiO<sub>2</sub> nanowires at the surface. Thus, the on-set potential shifting suggests high catalytic reactivity of the Au-NPs coated catalyst at relatively low overpotential. All Au-Mpy/Mpym NPs coated NanoCOT electrodes showed higher reactivity in presence of CO<sub>2</sub> in the solution compared to the bare NanoCOT electrode. Au-2Mpy/NanoCOT showed the best performance with a current density of 9000  $\mu$ A cm<sup>-2</sup> at -1.1 V vs RHE. However, the increase in current density of the catalysts in CO<sub>2</sub> saturated solution could also be due to increased proton reactivity as the pH of  $CO_2$  saturated solution (pH = 6.90 ± 0.10) is lower with higher  $H^+$  concentration compared to the  $N_2$  purged solution (pH = 9.57 ± 0.08). So, the rotating ring disk electrode (RRDE), a more efficient double-electrode hydrodynamic voltammetry technique, was applied to get a quick insight into the catalyst's  $CO_2$  reactivity and to probe reduced products.

Rotating ring disk electrode.—The rotating ring-disk electrode (RRDE) is a commonly used tool in electrochemistry to quickly understand the catalytic activity of a material of interest. 44,45 RRDE is used in this report to probe CO<sub>2</sub>-reduced products at the Pt ring electrode by scanning the ring electrode in an oxidation potential range while applying a constant reduction potential to reduce CO<sub>2</sub> at Au Mpy/Mpym NP's modified GCE disk electrode. Pt ring electrode was scanned from 0.01 V to 1.51 V vs RHE because CO2 reduced products including CO, CH<sub>3</sub>OH, and HCOOH oxidize at the Pt surface in this potential range.<sup>46</sup> When a reduction potential ≤ -0.5 V vs RHE was applied to the Au-2Mpy modified disk electrode, a characteristic Pt oxidation-reduction peak was observed at the Pt ring electrode without detectable oxidation peak for CO<sub>2</sub>RR products (Fig. 8). However, a characteristic oxidation peak for CO stripping at the Pt surface was appeared in the CVs of the Pt ring while the disk electrode is polarized at  $-0.6 \,\mathrm{V}$  vs RHE. The CO oxidation peak was increased with the increase of applied negative potential at the Au-2Mpy/GCE which indicates increased CO production at enhanced negative potential. Furthermore, PtO reduction current at 0.6 V vs RHE was observed to decrease and the Hadsorption/desorption peaks at 0.15 V vs RHE was disappeared with CO production at the disk electrode. This might be due to the adsorption of CO at the active catalytic sites of the Pt surface and interruption of H adsorption/desorption process. Additionally, characteristic CO oxidation peak at the Pt ring electrode was not observed in N<sub>2</sub> purged solution, which further suggests that the oxidation peak at the Pt ring was due to the oxidation of the product generated from the reduction of CO<sub>2</sub> at the disk electrode (Fig. S2). A control experiment with 15 mM 2Mpy in 0.1 M KHCO<sub>3</sub> solution at GCE shows low catalytic reactivity in CO2 purged solution compared to the N<sub>2</sub>-purged solution. Additionally, characteristic oxidation peak for CO2 reduced products were not observed during Pt ring electrode scan in  $CO_2$  purged 2Mpy solution even at -1.1 V vs RHE at GCE (Fig. S5). This observation implies that 2Mpy has no catalytic effect on electrochemical CO2 reduction. RRDE investigation of Au-2Mpym and Au-4Mpy has shown a similar oxidation peak at Pt ring electrode (Fig. S3). However, we did not

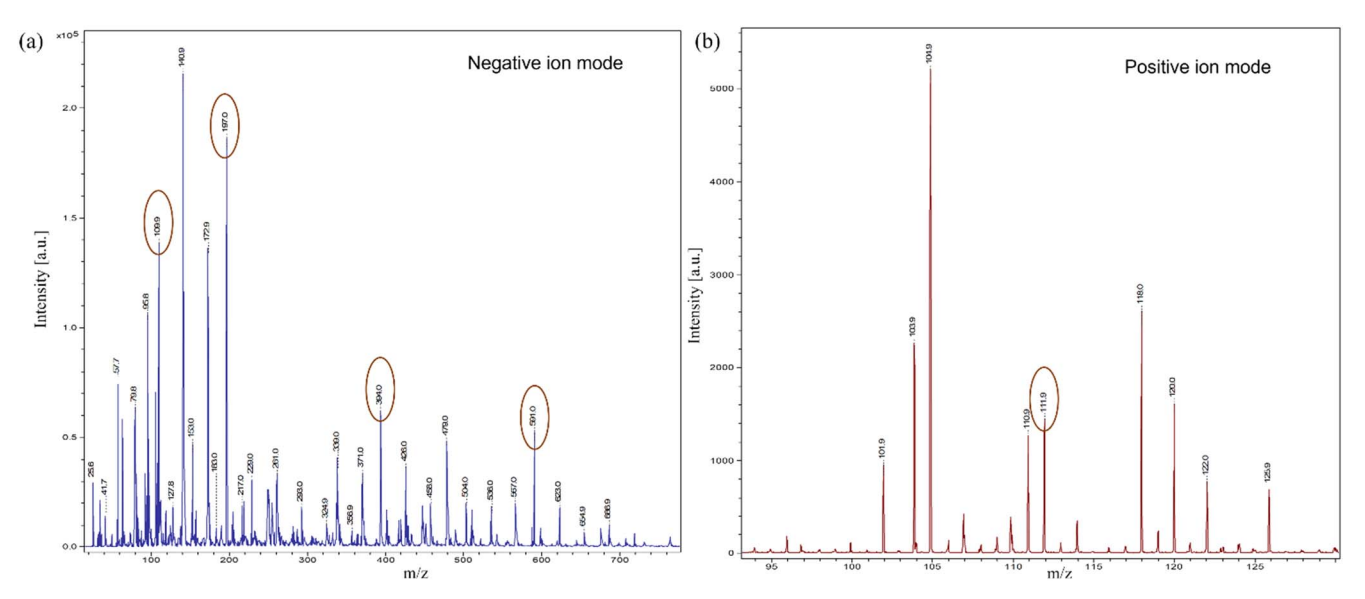
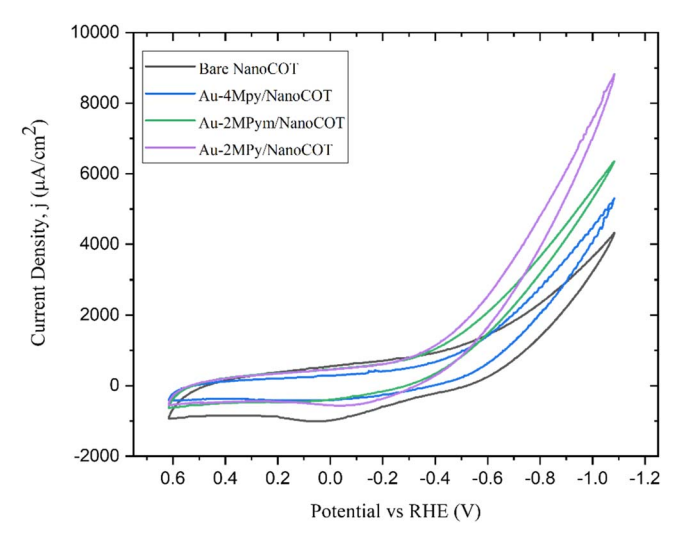


Figure 6. MALDI-TOF MS spectra of Au-2Mpy in negative (a) and positive (b) ion mode.



**Figure 7.** CVs of bare NanoCOT (black line), Au-2Mpy/NanoCOT (violet line), Au-2Mpym/NanoCOT (green line) and Au-4Mpy/NanoCOT (blue line) electrodes conducted in  $\rm CO_2$  saturated 0.1 M KHCO $_3$  solution. A spiral Pt wire was used as the counter electrode for the system. The scan rate was 100 mV s $^{-1}$ .

observe a characteristic double oxidation peak for HCOOH or CH<sub>3</sub>OH as shown in Fig. S4 during the Pt ring electrode scan at any applied negative potential at Au NP modified GCE which implies detectable HCOO<sup>-</sup>/HCOOH or CH<sub>3</sub>OH were not produced from CO<sub>2</sub> reduction at the disk electrode. We also test the catalytic formic acid oxidation activities of Au-2MPy in 0.1 M KHCO<sub>3</sub> (Fig. S10) as a control for future studies of the catalytic transformation of chemical fuels.

Faradaic efficiency.—Faradaic efficiency (FE) was used (Eq. 1) to quantify the catalytic activity and selectivity of the synthesized electrodes. The 2Mpy modified Au nanoparticle coated NanoCOT (Au-2Mpy/NanoCOT) electrode demonstrated the highest performance for  $CO_2$  reduction with 51.69% FE compared to Au-4Mpy or Au-2Mpym coated catalyst (Fig. 9a). However, the catalyst showed high selectivity for  $H_2$  production at low overpotential, for instance at -0.63 V vs RHE  $H_2$  FE is 56.09% (Fig. 9b). This is due to the facile kinetics of the proton reduction reaction. CO selectivity gradually increases with the increase of applied potential and reached the highest CO selectivity at -1.38 V vs RHE which might

Table III.	m/z values	and assigned	l ions for	MALDI-TOF	mass
spectrome	etry.				

m/z	Assigned ions
109.9	[C <sub>5</sub> H <sub>4</sub> NS] <sup>-</sup>
110.9	$[C_5H_5NS]^+, [C_4H_3N_2S]^-$
111.9	$[C_4H_4N_2S]^+, [C_5H_6NS]^+$
112.9	$[C_4H_5N_2S]^+$
197.0	Au
394.0	$Au_2$
591.0	$Au_3$
417.0	$[Au(C_5H_3NS)_2]^-$
419.0	$[Au(C_4H_3N_2S)_2]^-$
724.0	$[\mathrm{Au}_2(\mathrm{C}_5\mathrm{H}_4\mathrm{NS})_3]^-$

be due to increased potential facilitating CO2 reduction reaction at the catalyst surface at the specific potential. However, CO selectivity drops with the increase of potential after -1.38 V because of the mass transfer limitation of CO<sub>2</sub>RR for poor CO<sub>2</sub> solubility in an aqueous solution compared to H<sup>+</sup>. In contrast, 4-Mpy coated NanoCOT shows high H<sub>2</sub> selectivity at all applied potentials. However, the highest CO selectivity for this catalyst was observed at a relatively low overpotential at -0.88 V vs RHE compared to the Au-2Mpy/NanoCOT. Au-2Mpym/NanoCOT shows the poorest catalytic activity for CO<sub>2</sub>RR among all three catalysts. The highest CO FE for this catalyst is 19.92% at -0.88 V vs RHE. However, Au-2Mpym/NanoCOT shows the highest  $H_2$  production at -1.38 V vs RHE with a FE of 80.71%. A general trend was observed at all of the catalysts for H<sub>2</sub> and CO production: CO selectivity increase when H<sub>2</sub> production decrease. This is because CO<sub>2</sub> reduction reaction and proton reduction reaction are competitive reactions at the catalyst surface. For instance, CO production at Au-4Mpy/ NanoCOT electrode was observed to decrease with increased H<sub>2</sub> production at higher potentials than  $-0.88\,\mathrm{V}$  vs RHE. CO production at Au-4Mpy/NanoCOT catalyst was higher than the Au-2Mpym/NanoCOT but lower than the Au-2Mpy/NanoCOT catalyst. Both Au-2Mpym/NanoCOT and Au-4Mpy/NanoCOT showed high selectivity for H<sub>2</sub> production compared to the Au-2Mpy/NanoCOT catalyst. Additionally, the bare NanoCOT electrode shows the highest selectivity for H<sub>2</sub> production with a FE of 100% at -1.38 V vs RHE (Fig. S8). CO production was not observed at the bare NanoCOT electrode which implies that NanoCOT is only selective to H<sup>+</sup> reduction reaction. The total FE at low overpotential

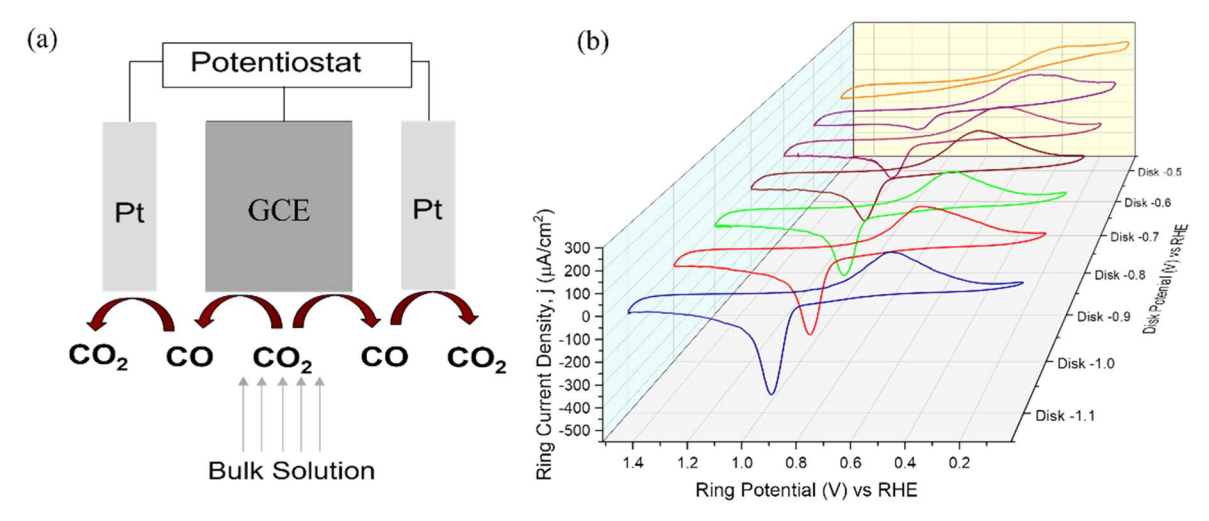


**Figure 8.** The schematic of RRDE setup for  $CO_2R$  product analysis (a) and CVs at Pt ring electrode in oxidation potential range (*X*-axis) at various constant reduction potential applied at the GCE (*Z*-axis) drop coated with Au-2Mpy NPs (b). Characteristic CO oxidation peak was not observed at -0.5 V vs RHE disk potential (orange line). CO oxidation peak was observed at -0.6 V vs RHE and/or high negative potential (violet line). The electrolyte was  $CO_2$  purged 0.1 M KHCO<sub>3</sub> solution. The counter electrode was spiral Pt wire, and 200 mV s<sup>-1</sup> scan rate was used in Pt ring scan.

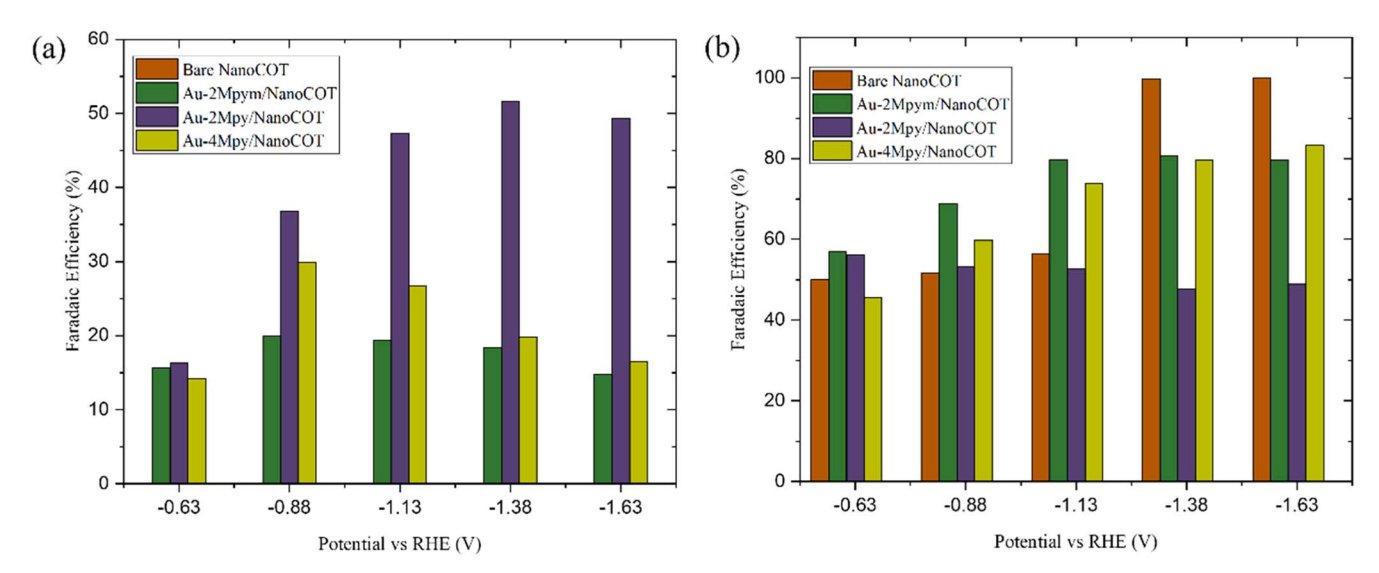


**Figure 9.** FE of CO<sub>2</sub> reduced products, (a) CO and (b) H<sub>2</sub> in CO<sub>2</sub> saturated 0.1 M KHCO<sub>3</sub> solution for bare NanoCOT (red bar), Au-2Mpy/NanoCOT (violet bar), Au-2Mpym/NanoCOT (green bar) and Au-4Mpy/NanoCOT (olive bar) electrode at various applied potential. A two-compartment, air-sealed electrochemical cell separated by a cation membrane was used for this study. The counter and reference electrodes were graphite rod and Ag/AgCl, respectively.

is not 100%, which might be due to the non-faradaic current for double-layer capacitance. Furthermore, at low overpotentials, a longer electrolysis time is required for desired charge accumulation. Longer electrolysis time without solution stirring might have induced a thick double layer at the catalyst surface. For instance, 2C charge accumulation at  $-0.63~\rm V$  vs RHE for Au-2Mpy/NanoCOT with a current density of  $1.50\pm0.15~\rm mA~cm^{-2}$  requires 20–25 min of electrolysis whereas at  $-1.63~\rm V$  vs RHE with a current density of  $14.37~\pm~0.54~\rm mA~cm^{-2}$  requires only 3–4 min of electrolysis. Thus, 100% total FE was observed at high potential.

In summary, the CO selectivity of the three Au NP-modified NanoCOT catalyst follow the trend of Au-2Mpy > Au-4Mpy > Au-2Mpym in this report. This CO<sub>2</sub>RR selectivity trend is considered to be associated with (1) NP size and surface coverage, (2) surface binding configurations of Mpy/Mpym on the Au NP surface, and (3) the relationship of the pKa of the passivating molecules with CO<sub>2</sub>RR product selectivity. High stability and small size distribution of Au-2Mpy NPs help them to disperse on the NanoCOT substrate surface with sufficient surface coverage to promote CO<sub>2</sub>RR reaction with minimum NanoCOT surface exposed. The well-dispersibility of NPs as shown by SEM and TEM images can justify the higher CO2 catalytic reactivity of Au-2Mpy than Au-4Mpy which forms micrometer sized aggregates on the NanoCOT. Au-2Mpym NPs show less selectivity than Au-4Mpy NPs although they were expected to have a higher selectivity for CO<sub>2</sub> reduction because of their smaller particle size, higher stability with improved surface coverage on the NanoCOT substrate than Au-4Mpy NPs. Previous works demonstrated that 2Mpy molecules have perpendicular orientation on Au surface<sup>47</sup> whereas 2Mpym molecule has a parallel orientation at the Au surface bonded with pyrimidine ring.<sup>48</sup> As parallel-oriented passivating molecules cover a large portion of the Au nano-surface, this could prevent the CO<sub>2</sub> molecule from reaching the Au surface due to steric hindrance. However, 4Mpy orientation can be perpendicular<sup>47</sup> or nearly parallel<sup>49</sup> to the Au surface. In addition, pKa values of the passivating molecule might have a large influence on the product selectivity. Table IV shows the pKa values and pH in an aqueous solution for 2Mpy, 4Mpy, and 2Mpym. 2Mpym has the lowest pKa value which means it has a high proton donation tendency and the lowest proton accepting ability than 2Mpy and 4Mpy molecules. These passivating molecules typically bind to Au surface by S atom and are in thion form. Low pKa value might induce low local pH and high local H+ concentration that can suppress CO<sub>2</sub> reduction at the electrode due to the competitive nature of both reactions. In contrast, 4 Mpy has a comparatively

Table IV. pKa and pH values of Au passivating molecules used in this study.

Passivating molecule	pKa <sup>Ref.</sup>	pH of 60 mM solution
2Mpy	9.81 <sup>50,51</sup>	7.41
4Mpy	8.65 <sup>50</sup>	6.83
2Mpym	$7.13^{51}$	5.71

higher pKa value from 2Mpym and shows moderate CO<sub>2</sub> reduction selectivity. Additionally, 2Mpy has the highest pKa and highest local pH, which might be the reason for the highest CO selectivity compared to the other two catalysts. To conclude, all factors including NP size, and surface coverage, the surface binding configuration of Mpy/MPym, and their acidity should be considered for their synergistic effect on CO<sub>2</sub>RR selectivity.

NanoCOT stability test.—Electrolytic CO2RR requires a water oxidation reaction to supply electrons in a 2-electrode configuration. As shown in our early publication, NanoCOT can be utilized as an anode for catalytic water oxidation.<sup>25</sup> An electrochemical H-cell for efficient CO<sub>2</sub>RR and water splitting reaction was prepared by using Au-2Mpy/NanoCOT as cathode and bare NanoCOT electrode as anode. Chronoamperometry (CA) was used to examine the stability of the catalyst in the system. Au-2Mpy/NanoCOT was chosen as the cathode since it has the highest catalytic activity for CO<sub>2</sub>RR. The measurement was carried out in a three-electrode system using Ag/ AgCl as a reference electrode. CO2 gas was purged through the cathode compartment of the H-cell during the electrolysis at a flow of 50 ml min<sup>-1</sup> from the bottom of the working electrode into the electrolyte solution containing 0.1 M KHCO<sub>3</sub>. Our first experiment was carried out in a two-compartment electrochemical cell separated by Nafion 117 membrane of 0.64 cm<sup>2</sup> in diameter (Fig. 10a). The applied potential was -1.38 V vs RHE as Au-2Mpy/NanoCOT showed the highest CO production at that potential. Au-2Mpy/ NanoCOT showed good stability with a current density ~10 mA cm<sup>-2</sup> up to 18.75 C charge collection. However, the current density sharply decreased with time after 18.75 C charge collection because of large gas bubble accumulation at the membrane at the cathode side, which limits ion flow through the membrane and reduces current density. To avoid the ion flow limitation, CA was also conducted in a one-compartment, three-electrode cell using Au-

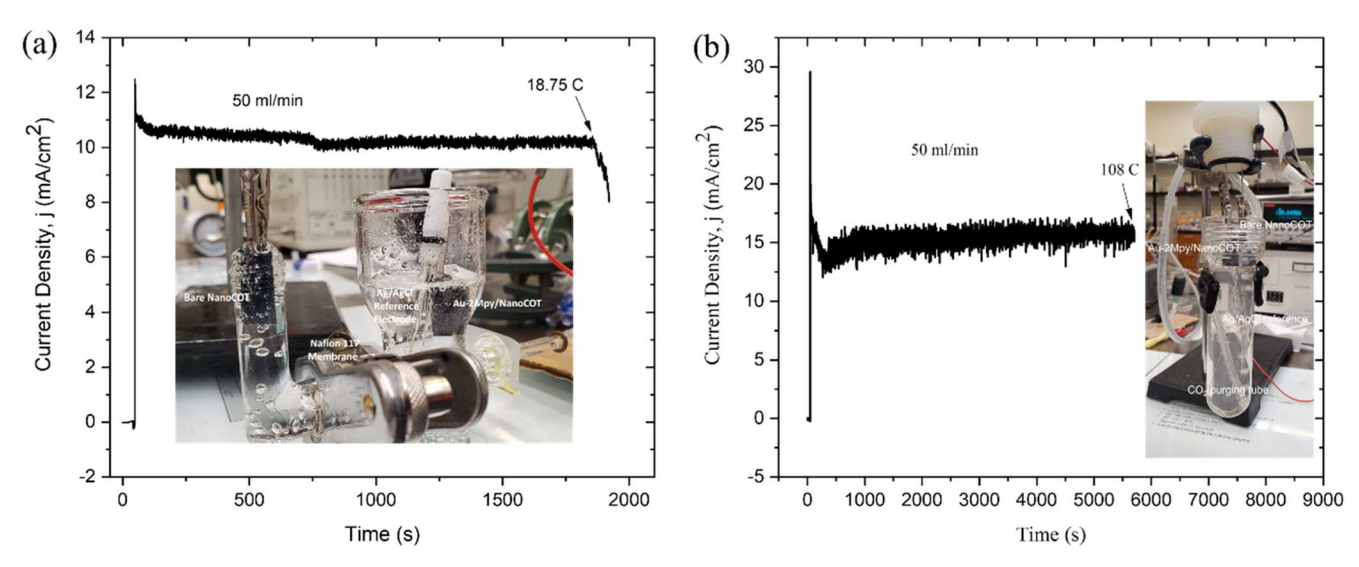


Figure 10. Chronoamperometric measurement of Au-2Mpy/NanoCOT electrode for durability test. (a) 18.75 C charge collection with a current density ∼10 mA cm<sup>-2</sup> in the two-compartment electrochemical cell and (b) 108C charge collection with a current density ~15 mA cm<sup>-2</sup> in one compartment electrochemical cell. Inset is the three-electrode cell setup with Au-2Mpy/NanoCOT working electrode, bare NanoCOT counter electrode, and Ag/AgCl reference electrode in a two-compartment electrochemical cell separated by cation exchange membrane (a) and one compartment electrochemical cell (b).

2Mpy/NanoCOT, bare NanoCOT, and Ag/AgCl electrodes as the working, counter, and reference electrodes, respectively. The current density increased in this new set up which is likely due to the proximity of electrodes and lack of membrane-induced ion transport limitation. Specifically, the electrode shows good stability with a current density of  $\sim$ 15 mA cm<sup>-2</sup> at -1.38 V vs RHE when 108 C of charge was collected in this system (Fig. 10b).

#### Conclusions

The bare NanoCOT electrode is only selective in producing H<sub>2</sub> with no detectable CO2 reduction. Surface modification of NanoCOT substrate with Au-2Mpy/Au-2Mpym/Au-4Mpy NPs shows CO<sub>2</sub> activity with various CO and H2 selectivity. Au-2Mpy NPs-modified NanoCOT provides the highest CO FE among all three Au-NP catalysts with the lowest hydrogen evolution reaction activity. Au-2Mpym/NanoCOT and Au-4Mpy/NanoCOT catalysts show high selectivity for H<sub>2</sub> production. Dispersity of AuNPs on NanoCOT, passivating molecule orientations, and pKa values are considered to have a synergistic effect on catalyst selectivity. Generally, a CO<sub>2</sub>RR product selectivity trend is observed for all the catalysts: CO selectivity is inversely related to the H<sub>2</sub> selectivity for the competitive nature of both reactions at the catalyst surface. CO production at low overpotentials is low likely because of the slow reaction kinetics. With the increase of potential, the CO selectivity started to increase. However, H<sub>2</sub> production is dominating at a very high potential because of the low mass transport of CO<sub>2</sub> to the catalyst surface. CH<sub>3</sub>OH formation is not observed on the Mpy/Mpym derivative modified Au nanoparticle coated catalyst. In summary, we have synthesized a novel NanoCOT catalyst modified with Au-Mpy/ Mpym NPs for CO<sub>2</sub>RR that can reduce CO<sub>2</sub> into CO and H<sub>2</sub> in aqueous solution without detectable liquid product formation and demonstrated a durable electrochemical cell made of NanoCOT anode and Au-2Mpy/NanoCOT cathode for CO2 electrocatalysis with a current density of  $\sim$ 15 mA cm<sup>-2</sup>. Additionally, we have demonstrated an online GC system for gaseous product analysis from CO2 reduction reaction, which includes a pressure monitoring system for accurately determining gaseous product by monitoring gaseous product formation and helping to investigate any leakage of the system.

## Acknowledgments

S.P. acknowledges the support of Marilyn Williams Elmore and John Durr Elmore Professor fellowship. We acknowledge National Science Foundation (NSF) for supporting this work under Award Number CBET-2113505. We thank the support of the "new" transportation research fund from the Alabama Transportation Institute. We also acknowledge the support of the grant NSF CHE-1726812 from the Major Research Instrumentation Program for the purchase of the MALDI/TOF-TOF mass spectrometer.

## **ORCID**

Md Ashaduzzaman https://orcid.org/0000-0002-0445-1736 Lyndi Strange https://orcid.org/0000-0001-6346-7423 Shanlin Pan (b) https://orcid.org/0000-0003-2226-9687

# References

- 1. (2022), CO<sub>2</sub>.Earth, 2022, May Global CO<sub>2</sub> Emissions.
- 2. J. Shi, Y. Jiang, Z. Jiang, X. Wang, X. Wang, S. Zhang, P. Han, and C. Yang, Chem. Soc. Rev., 44, 5981 (2015).
- 3. D. D. Zhu, J. L. Liu, and S. Z. Qiao, Adv. Mater., 28, 3423 (2016).
- S. N. Habisreutinger, L. Schmidt-Mende, and J. K. Stolarczyk, Angew. Chem. Int. Ed. Engl., 52, 7372 (2013).
- W. Wang, S. Wang, X. Ma, and J. Gong, Chem. Soc. Rev., 40, 3703 (2011).
   M. G. Kibria, J. P. Edwards, C. M. Gabardo, C. T. Dinh, A. Seifitokaldani, D. Sinton, and E. H. Sargent, Adv. Mater., 31, e1807166 (2019).
- 7. J. Schneider, H. Jia, J. T. Muckerman, and E. Fujita, Chem. Soc. Rev., 41, 2036
- 8. C. Chen, J. F. Khosrowabadi Kotyk, and S. W. Sheehan, Chem, 4, 2571 (2018).
- D.-R. Yang, L. Liu, Q. Zhang, Y. Shi, Y. Zhou, C. Liu, F.-B. Wang, and X.-H. Xia, Sci. Bull., 65, 796 (2020).
- 10. J. Rosen, G. S. Hutchings, Q. Lu, S. Rivera, Y. Zhou, D. G. Vlachos, and F. Jiao, ACS Catal., 5, 4293 (2015).
- 11. J. Jiao et al., Nat. Chem., 11, 222 (2019).
- 12. W. Liu et al., Nat. Commun., 13, 1877 (2022).
- 13. Z. Geng, X. Kong, W. Chen, H. Su, Y. Liu, F. Cai, G. Wang, and J. Zeng, Angew. Chem. Int. Ed. Engl., 57, 6054 (2018).
- 14. L. E. Strange, J. Yadav, X. Li, and S. Pan, J. Electrochem. Soc., 167, 146518
- 15. J. Qiao, Y. Liu, F. Hong, and J. Zhang, Chem. Soc. Rev., 43, 631 (2014).
- 16. H. Lee, RSC Adv., 4, 41017 (2014).
- 17. Q. Zhu, X. Sun, D. Yang, J. Ma, X. Kang, L. Zheng, J. Zhang, Z. Wu, and B. Han, Nat. Commun., 10, 3851 (2019).
- 18. W. Zhu, R. Michalsky, O. Metin, H. Lv, S. Guo, C. J. Wright, X. Sun, A. A. Peterson, and S. Sun, J. Am. Chem. Soc., 135, 16833 (2013).
- 19. Q. Yu, X. Meng, L. Shi, H. Liu, and J. Ye, Chem. Commun. (Camb), 52, 14105 (2016).
- 20. A. A. Peterson and J. K. Nørskov, J. Phys. Chem. Lett., 3, 251 (2012).
- 21. J. Zhang, P. Zhou, J. Liu, and J. Yu, Phys. Chem. Chem. Phys., 16, 20382 (2014).
- A. Dhakshinamoorthy, S. Navalon, A. Corma, and H. Garcia, Energy Environ. Sci., 5, 9217 (2012).
- Y. Yang, Y. Ling, G. Wang, T. Liu, F. Wang, T. Zhai, Y. Tong, and Y. Li, Nano Lett., 15, 7051 (2015).
- 24. J. Wu et al., Nat. Commun., 7, 13869 (2016).

- A. Al Mayyahi, B. M. Everhart, T. B. Shrestha, T. C. Back, and P. B. Amama, *RSC Adv.*, 11, 11702 (2021).
- Z. Shan, P. S. Archana, G. Shen, A. Gupta, M. G. Bakker, and S. Pan, J. Am. Chem. Soc., 137, 11996 (2015).
- 27. Y. Fang and J. C. Flake, J. Am. Chem. Soc., 139, 3399 (2017).
- S. I. Rybchenko, D. Touhami, J. D. Wadhawan, and S. K. Haywood, *Chem. Sus. Chem.*, 9, 1660 (2016).
- 29. E. E. Barton, D. M. Rampulla, and A. B. Bocarsly, *JACS*, 130, 6342 (2008).
- C. Costentin, J. C. Canales, B. Haddou, and J. M. Saveant, J. Am. Chem. Soc., 135, 17671 (2013).
- 31. J. Yuan, L. Zheng, and C. Hao, RSC Adv., 4, 39435 (2014).
- A. B. Bocarsly, Q. D. Gibson, A. J. Morris, R. P. L'Esperance, Z. M. Detweiler, P. S. Lakkaraju, E. L. Zeitler, and T. W. Shaw, ACS Catal., 2, 1684 (2012).
- J. H. Jeon, P. M. Mareeswaran, C. H. Choi, and S. I. Woo, RSC Adv., 4, 3016 (2014)
- Z. Ma, C. Lian, D. Niu, L. Shi, S. Hu, X. Zhang, and H. Liu, *Chem. Sus. Chem.*, 12, 1724 (2019).
- 35. J. J. Walsh, *Phys. Chem. Chem. Phys.*, **22**, 12766 (2020).
- 36. M. Abdinejad et al., ACS Catal., 12, 7862 (2022).
- 37. A. J. Lucio and S. K. Shaw, J. Phys. Chem. C, 119, 12523 (2015).

- 38. P. K. Giesbrecht and D. E. Herbert, ACS Energy Lett., 2, 549 (2017).
- A. A. Ensafi, H. A. Alinajafi, M. Jafari-Asl, and B. Rezaei, J. Electroanal. Chem., 804, 29 (2017).
- 40. S. I. Rybchenko, D. Touhami, J. D. Wadhawan, and S. K. Haywood, *ChemSusChem*, 9, 1660 (2016).
- H.-L. Zhang, S. D. Evans, J. Henderson, R. E. Miles, and T. Shen, *J. Phys. Chem. B*, 107, 6087 (2003).
- 42. A. M. Keene and K. M. Tyner, J. Nanopart. Res., 13, 3465 (2011).
- 43. J. H. Elizabeth Dyer, Z. Shan, and S. Pan, ECS Trans., 77, 61 (2017).
- 44. F. Zhang and A. C. Co, J. Electrochem. Soc., 167, 046517 (2020).
- 45. I. Palm et al., ACS Appl. Energy Mater., 5, 2949 (2022).
- X. Zhu, K. Gupta, M. Bersani, J. A. Darr, P. R. Shearing, and D. J. L. Brett, *Electrochim. Acta*, 283, 1037 (2018).
- 47. S. F. Takahiro, M. Y. Soichiro, and T. Isao, Electrochimica Acta, 45, 2861 (2000).
- 48. M. L. A. T. L. S. Pinheiro, Surf. Sci., 441, 53 (1999).
- 49. L.-J. Wan, Y. Hara, H. Noda, and M. Osawa, *J. Phys. Chem. B*, **102**, 5943 (1998).
- R. A. Jones and A. R. Katritzky, Journal of the Chemical Society (Resumed), (0), 3610 (1958).
- H. J. Gais, T. Jagusch, N. Spalthoff, F. Gerhards, M. Frank, and G. Raabe, *Chem.*, 9, 4202 (2003).